2024 IEEE/RSJ International Conference on Intelligent Robots and Systems (IROS)
October 14-18, 2024. Abu Dhabi, UAE

Head-Mounted Hydraulic Needle Driver for Targeted Interventions in Neurosurgery

Zhiwei Fang, Chao Xu, Huxin Gao, Danny Tat-Ming Chan, Wu Yuan*, Hongliang Ren*

***Abstract*— Needle interventions are crucial in neurosurgery, requiring high precision and stability. This paper presents a 5-DoF head-mounted hydraulic needle robot designed for accurate and targeted needle insertion and neuroimaging in the deep brain. The robot is compact and lightweight by utilizing a hydraulic pipe transmission to connect the needle driver and actuator. The syringe pistons serve as the actuator and executor, enabling synchronized motion, minimal hysteresis, and high-accuracy insertion. The hydraulic transmission system exhibits hysteresis of less than 0.8 mm, with bidirectional insertion accuracy of approximately 0.05 mm. The resulting needle driver features a compact structure measuring 48 mm × 25 mm × 9 mm, accompanied by a 70-mm-long needle guide. The needle driver is mainly 3D printed, while the hydraulic transmission ensures full compatibility with magnetic resonance imaging (MRI) by isolating all electromagnetic parts from the executor. This compact and lightweight robot-assisted needle intervention system significantly enhances the safety, accuracy, and effectiveness of deep-brain neuroimaging. The feasibility of precise positioning and insertion is further demonstrated by deploying an optical coherence tomography (OCT) microneedle in a rat brain.**

I. Introduction

Neurosurgery is a complex and time-consuming operation and requires highly skilled neurosurgeons. Neurosurgeons face everlasting challenges, such as unstable human conditions, limited tissue accessibility, long operation time, and high stress. [1]. A robot-assisted neurosurgery system enables precise and robust operation and offers multiple benefits, including improved efficiency, increased accuracy, and reduced costs [2]. A number of surgical robots have been reported to provide precise and stable needle positioning and insertion in a minimally invasive manner [2]–[5]. However, most of these systems are based on robot arms and have bulky system volumes. Their table-mounting configurations require the patient to maintain a consistent relative position between the patient and the surgical system during the operation [6], [7], although patient movement is unavoidable during the actual procedure. By directly attaching a lightweight robot to the patient, the body-mounted systems have successfully demonstrated to reduce the errors caused by patient movements [8]–[10].

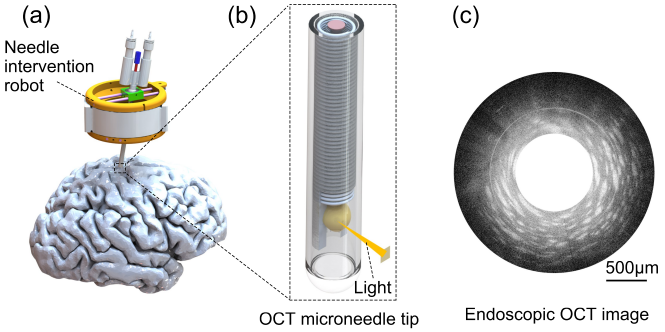

Fig. 1. Needle intervention robot equipped with an OCT microneedle. (a) Needle intervention robot for neurosurgery. (b) OCT microneedle tip. (c) Typical cross-sectional OCT image acquired in rat brain.

On the other hand, Magnetic resonance imaging (MRI) is crucial in neurosurgery as it offers real-time intraoperative images. Due to the magnetic field generated during MRI operation and the limited space within the MRI bore, developing compact MRI-compatible robotic systems is imperative [11]. Previously, we developed a 4 degrees of freedom (DoFs) needle positioner with a remote center of motion (RCM) recommendation system, which is compact, portable, and MRI-compatible [12], [13]. In this work, we further develop a hydraulic needle driver to fully actuate 5-DoFs head-mounted robotic needle interventions, such as neuroimaging. Most current needle drivers employ motor and gear mechanisms, resulting in larger structural dimensions and increased weight [14]. Moreover, these electromagnetic components hinder their integration with MRI for intraoperative imaging and navigation. To keep the robot lightweight and MRI-compatible, a long-distance transmission method is proposed to isolate the actuation system and its associated electromagnetic components from the needle driver.

While the tendon-driven mechanisms (TSM) is the most popular among commercial and research-oriented surgical robots, they exhibit noticeable force loss along the routing path during long-distance transmission, and the hysteresis profile varies with different layouts. Pressure-driven methods are gaining popularity in surgical robotics due to their conformability, flexibility, and effective force transmission

This work was supported in part by Hong Kong Research Grants Council (RGC) Collaborative Research Fund (CRF C4026-21GF and CRF C4063-18G), General Research Fund (ECS24211020, GRF14203821, GRF14216222, GRF 14216022), NSFC/RGC Joint Research Scheme N-CUHK420/22, Shenzhen-Hong Kong-Macau Technology Research Programme (Type C) Grant 202108233000303, the Innovation and Technology Fund (ITF) of Hong Kong SAR (ITS/240/21), the Science, Technology and Innovation Commission (STIC) of Shenzhen Municipality (SGDX20220530111005039), Guangdong Basic and Applied Basic Research Foundation (GBABF) #2021B1515120035.

Z. Fang, H. Gao, and H. Ren are with the Department of Electronic Engineering, The Chinese University of Hong Kong (CUHK), Hong Kong, China.

C. Xu and W. Yuan are with the Department of Biomedical Engineering, The Chinese University of Hong Kong (CUHK), Hong Kong, China.

Danny T.M. Chan is with the Department of Surgery, Chinese University of Hong Kong

Correspondence to: Wu Yuan: wyuan@cuhk.edu.hk; and Hongliang Ren: hlren@ieee.org.

capability [15]–[17]. Compared with pneumatic actuation, hydraulic actuation offers stabler transmission and quicker response. Therefore, we adopt the hydraulic actuation in the proposed system for motion and force transmission. Due to the additional need for flow sensors and the generation of noise in conventional pump-based actuators [18], we further propose a syringe-based actuation method to utilize a pair of syringes and their pistons connected by the hydraulic pipe for motion and force transmission. Furthermore, a lead screw is employed to enhance the accuracy and stiffness of the system.

As the main contribution of this study, we develop a hydraulic-driven 2-channel needle driver that provides high needle insertion accuracy and stability. We investigate the hysteresis effect of hydraulic transmission and the performance of motion and force transmission. The needle driver demonstrates high insertion accuracy and stiffness and has a compact form size. Additionally, since both the robot positioner and needle driver are MRI-compatible, this robot has the potential to utilize MRI guidance for novel surgical navigation. As an emerging medical imaging modality, optical Coherent Tomography (OCT) provides micrometer-resolution and video-rate 3D imaging of tissue in real-time [19]–[25]. To demonstrate the robotic needle procedures, we integrate an OCT microneedle [26] and perform the neuroimaging in a rat brain.

II. Robot Design and System Setup

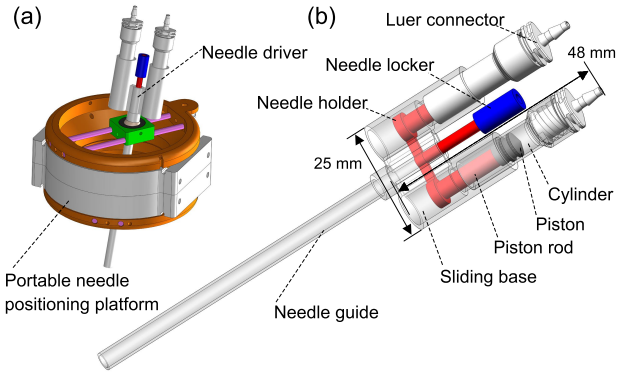

Fig. 2. Needle intervention robot. (a) Needle positioner with an integrated needle driver. (b) Semi-perspective image of the piston-based needle driver.

Fig. 2(a) illustrates the schematic design of the proposed needle intervention robot. A newly developed needle driver is installed on the previously developed needle positioner [12] to enable full actuation of the needle. To implement the portable and MRI-compatible design, the piston-based needle driver is actuated by the hydraulic pipe, and the motor part is isolated from the executor.

A. Mechanism Design

The hydraulic pistons serve as the core mechanism of the needle driver, as depicted in Fig. 2(b). As the pistons slide within the cylinder tubes, the needle is held by the needle locker and moves with the pistons. The needle locker is installed on the top of the needle holder to secure the needle holder and the needle. The needle holder moves within the sliding base, which is installed on the needle positioner. A long needle guide (70 mm in the prototype version) connects the needle driver and the needle positioner while allowing the needle orientation to change along with the positioner. To apply a uniform force on the needle driver and avoid errors caused by directional biases, a symmetrical double-channel design is proposed to enhance the stability of the needle driver.

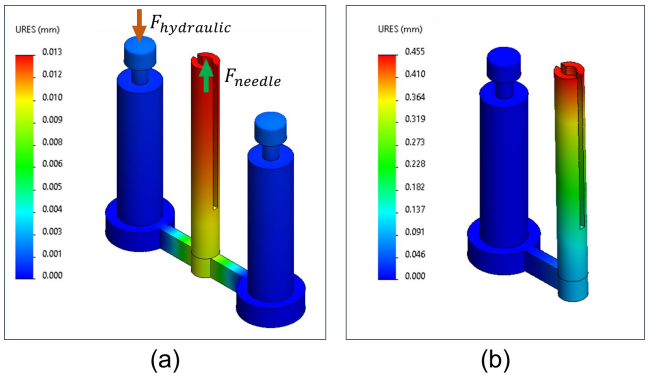

Fig. 3. Simulation comparison of double-channel and single-channel needle holder.

Fig. 3 shows the simulation results of double-channel and single-channel needle holders (only one $F_{hydraulic}$ is shown for simplicity while each piston is pushed by hydraulic). The torque generated by the asymmetric design of the single-channel causes the axis of the needle driver to deviate from the original axis. When both $F_{hydraulic}$ and F_{needle} are 2 N, the displacement at the upper end of the needle holder is approximately 0.4 mm. However, the double-channel needle driver produces almost no deviation along the axis.

B. Manufacturing

The major part of the needle driver is 3D printed (J826, Stratasys Inc.), and then assembled with luer syringes.

1) 3D printing: The sliding base, needle holder, piston rod, and needle guide are 3D printed as a whole with polylactic acid (PLA) material. The printer uses a soluble support material (No. SUP706B) and prints three-dimensional hollow structures. After printing, the object is rinsed with water to remove the bulk support material, followed by two hours of immersion in a NaOH solution. Consequently, the support material between the sliding base and needle holder softens and is easily removed by the water flow.

This integrated 3D-printed hollow structure eliminates the need for additional assembly connections, thereby reducing potential assembly errors. Unlike the traditional methods using rigid support materials, the soluble support material provides a smooth surface after the aforementioned process. This allows the needle holder to slide smoothly within the sliding base. The thickness of the support material is set to be 1 mm, as this thickness allows for easy removal of all the support material and does not cause noticeable shaking

during sliding. The overall size of the needle driver without considering the needle guide is 48 mm×25 mm×9 mm, and the weight is 50 g.

2) Syringe assembling: We use custom cylinders and pistons adapted from the standard 1 ml luer syringe with a female luer connector. The inner diameter of the channel on the sliding base is designed to be 6.85 mm, allowing the cylinder to be plugged into the needle holder and secured with glue. Then, the female luer connector of the syringe is connected to a male luer connector with a pipe attached to it.

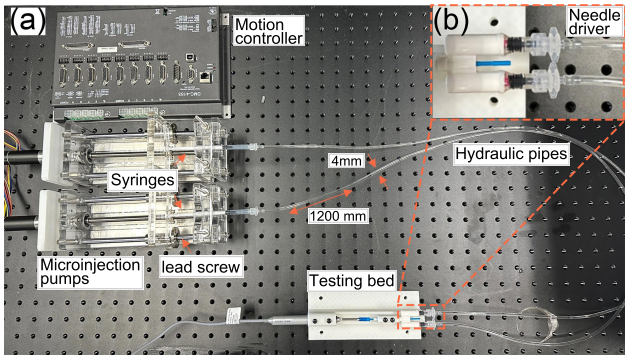

Fig. 4. (a) Overview of the needle driver system, comprised of the proximal side lead screw-driven syringes, distal side needle driver, and the motion control board. Two 1200-mm-long pipes connect the proximal and distal syringes. (b) The distal side needle driver.

C. Actuation

The distal pistons are connected to the proximal side by a 2-channel pipe (1200 mm×4 mm×2.5 mm) as shown in Fig. 4(a). The actuation part of the needle driver contains two microinjection pumps. The pumps are actuated by brushless servo motors (gear ratio 75.9:1, encoder resolution 4096). The motor is controlled and encoded by a motion control board (DMC-4183, Galil Motion Control Inc.). A lead screw mechanism widely adopted in microfluidic applications for its high accuracy converts motor rotation into linear translation. The luer syringe cylinder is fixed to the lead screw base and the piston rod is attached to the lead screw. The syringes on both sides are the same size, so the movement of the distal side is the same as that of the proximal side. Since the resolution of the motor encoder is 4096 and the lead of the screw is 1 mm, the ideal insertion resolution of the needle driver is around 2 μm.

III. Mathematical Modeling

The syringes on the proximal and distal sides are the same, so ideally, the movement on both is synchronized. However, due to different constraints on the two sides and the hydraulic transmission characteristics, this section establishes a dynamic system model to investigate the distal side response. The system model contains two parts: piston motion dynamics and pipe hydrodynamics.

The connecting pipe is assumed to be non-deformable during the motion, and the fluid is assumed to be incompressible and inviscid in the connecting pipe. These assumptions are valid since the diameter of the connecting pipe is small, as well as the volume of the fluid [27].

A. Piston Dynamics

Governed by Newton's second law, the proximal and distal governing equations of the pistons differ from the boundary constraints. From the non-deformable connecting pipe assumption, the pistons are lumped into one rigid body, as shown in Fig. 5. For simplicity, the diagram only shows the pushing stage when the needle moves forward.

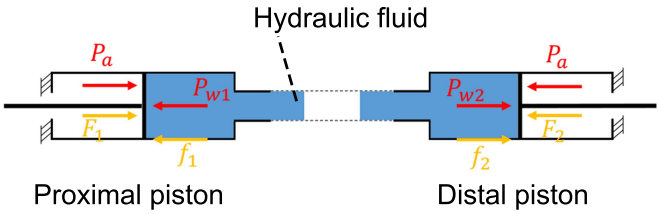

Fig. 5. Dynamics diagram of the piston pair. The proximal and distal pistons are subjected to similar types of forces, including hydraulic pressure, atmospheric pressure, friction forces, and contact forces on the piston rods.

For proximal piston dynamics, the governing equation is shown as follows:

$$\begin{aligned} \ddot{x}_1 &= \frac{F_{a1} + F_1 - F_{w1} - F_{f1}}{M} \\ x_1 &= f(t) \\ \dot{x}_1 &= \dot{f}(t), \end{aligned} \tag{1}$$

where x_1, $\dot{x}_1$, and $\ddot{x}_1$ represent the proximal piston displacement, velocity, and acceleration, respectively. M is the piston mass. P_a is the atmospheric pressure around the piston rod and P_{w1} is the hydraulic pressure in the hydraulic circuit. Being linked to the lead screw rod, F_1 is the push force on the piston, and $f(t)$ is the piston displacement which is the same as the lead screw. f_1 is the friction force. The analysis on the distal side is mostly the same, except that F_2 is contact force during the insertion.

B. Hydrodynamics

For flow in a pipe, the Reynolds number is generally defined as:

$$Re = \frac{\rho u D_H}{\mu}, \tag{2}$$

where ρ is the density of the fluid ($1.0{\times}10^3$ kg/m for water in 25°), μ is the dynamic viscosity of the fluid ($0.8937{\times}10^{-3}$ $N \cdot s/m^2$ for water in 25°). u is the velocity of the fluid. D_H is the inner diameter of the circular pipe. Considering the average velocity equals 0.5 mm/s and the pipe inner diameter equals 2.5 mm,

$$Re \approx 1.399, \tag{3}$$

which indicates that the hydraulic pipe is in the laminar flow state. Then, based on the steady flow assumption in hydrodynamics, we use the Bernoulli principle to describe the hydraulic dynamics. Consider any fluid body in the body

with pressure p_1 and p_2 on each side. Then the Bernoulli equation is :

$$z_1 + \frac{p_1}{\rho g} + \frac{U^2}{2g} = z_2 + \frac{p_2}{\rho g} + \frac{U^2}{2g} + h_w, \tag{4}$$

where z_1 and z_2 is the fluid height on each side. h_w is the energy loss during the transmission. $U = Q/A$, where Q is the volumetric flow rate and A is the pipe's cross-sectional area. With the assumption of steady flow, the pipes are almost horizontal, and there is no local loss because the pipes are non-deformable. We have $z_1 = z_2$, $U_1 = U_2$, and $h_w = h_f$, respectively. h_f is the frictional transmission loss. Hence,

$$h_f = \frac{p_1 - p_2}{\rho g}. \tag{5}$$

On the other hand, with no acceleration on the steady flow body,

$$(p_1 - p_2) \cdot \pi r^2 = \tau \cdot 2\pi r \cdot L, \tag{6}$$

where τ is the friction force on the fluid body. From Newton's inner friction law for laminar flow,

$$\tau = \mu \frac{du}{dr}, \tag{7}$$

where u is the fluid velocity along the radial direction and is defined as:

$$u = \frac{Q}{\pi r^2}. \tag{8}$$

Combining (5), (6), (7), integrate u along the radial direction and consider the boundary condition that $u(r) = 0$, u is given as:

$$u = -\frac{\rho g h_f}{4\mu L}(r^2 - {r_0}^2). \tag{9}$$

Then, combining (8) and (9), Q is obtained using integration as follows:

$$Q = \frac{\pi \rho g h_f}{8\mu L} {r_0}^4. \tag{10}$$

IV. Transmission Performance Test

To validate the proposed design for OCT microneedle insertion, there are two key considerations regarding transmission performance:

- Analysis of hysteresis in the hydraulic drive system: This evaluation examined the behavior of the hydraulic drive system, specifically focusing on hysteresis. The results demonstrated the needle driver's ability to perform precise reciprocating movements, ensuring accuracy and reliability during the insertion process.

- Comparison of puncture forces: To assess the needle driver's capability for puncturing during surgical procedures, several common puncture forces encountered in surgery were compared. By conducting this comparison, we were able to validate the needle driver's effectiveness and suitability for puncturing, further confirming its potential for use in intervention applications.

A. Hysteresis Analisis

A linear sensor (KPM12R1, MIRAN) was attached to the distal end of the plastic bin, viewed as the needle tip, as shown in Fig. 6(a). Hysteresis is a common phenomenon in hydraulic, cable, and piezo-driven systems and is a major problem for such robots that require high accuracy [28]. The hysteresis of the hydraulic proximal-distal piston pair was measured in different displacement units and depicted in Fig. 6. The motors were controlled by the embedded PID controller to follow the triangle trajectory with a velocity of 0.5 mm/s, covering 80% of stroke length. The needle tip displacement has shown a steady speed area and hysteresis. The hysteresis value remains constant throughout the loop and the average value is 0.8 mm.

Then, a needle step insertion test was conducted using the measured hysteresis value. The needle was controlled to follow a step trajectory where it started from the initial point, advanced by increments of 3 mm, 4 mm, 5 mm, and

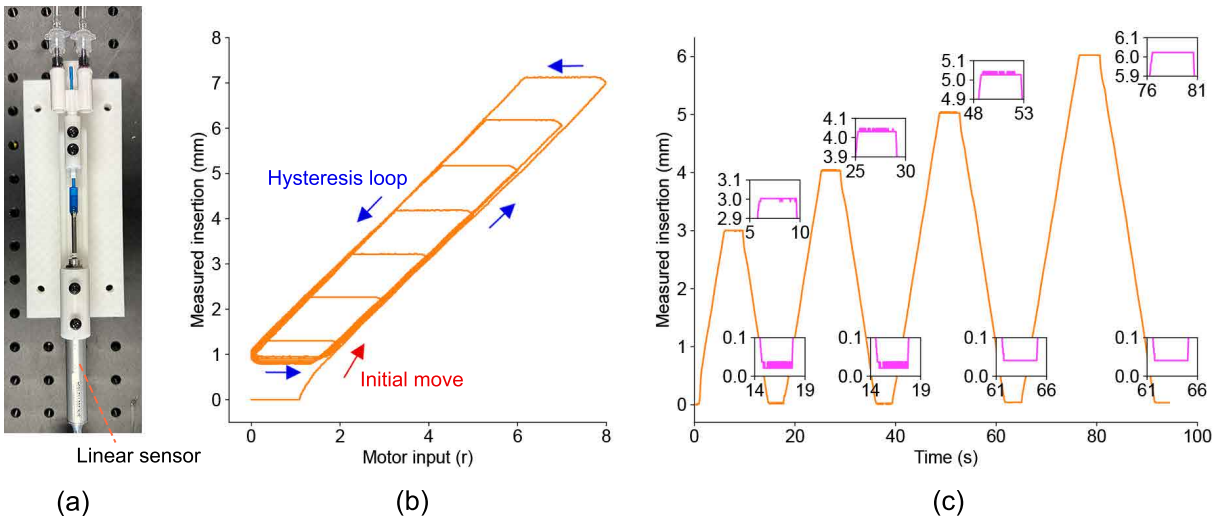

Fig. 6. Performance test of displacement transmission. (a) Experimental setup. (b) Hysteresis of the hydraulic-driven needle driver. The average hysteresis is about 0.8 mm. (c) Back-and-forth motion loop, using the measured hysteresis characteristic. The absolute error of the bi-directional insertion is less than 0.05 mm.

6 mm, and retracted back to the initial point after each step. As shown in Fig. 6 (c), the max error during the motion loop is less than 0.05 mm. These results prove the capability of the needle driver to achieve precise positioning at any point within the stroke length.

B. Force Transmission

The force transmission profile was recorded using a load-cell (AT8301, AUTODA) to validate the feasibility of the needle driver to perform puncturing. In this experiment, a plastic bin was held and inserted to contact the loadcell. At first, the tip of the plastic bin was put 1 mm away from the surface of the loadcell. Then the needle driver moved forward by 7 mm and remained stationary for 10 s at that position before retracting back to its original position. During this process, the loadcell recorded the changes in contact force as the needle tip approached and separated from the loadcell. The contact force recorded by the loadcell represents the magnitude of the puncturing force exerted by the needle driver. Fig. 7 depicts the changes in force during the process. As the needle driver moved forward, the contact force naturally increased due to the compression of the fluid. In the experiment, the maximum force reached 6.94 N. It then decreased to a stable value of around 5.1 N, which may be attributed to the hydraulic transmission entering a steady state after the needle driver stops moving. Finally, as the needle driver moved back, the contact force gradually decreased to 0 N. We compared with several clinically typical needle-tissue interaction forces [29]–[31] (as shown in Fig. 7) and found that this needle driver can perform the majority of clinical puncturing tasks and is capable of puncture intra-organ tissues (such as the brain tissue, heart, liver, etc.) with minimal compression. A phantom study showing the OCT microneedle going into gelatin is also done (see the supplement video).

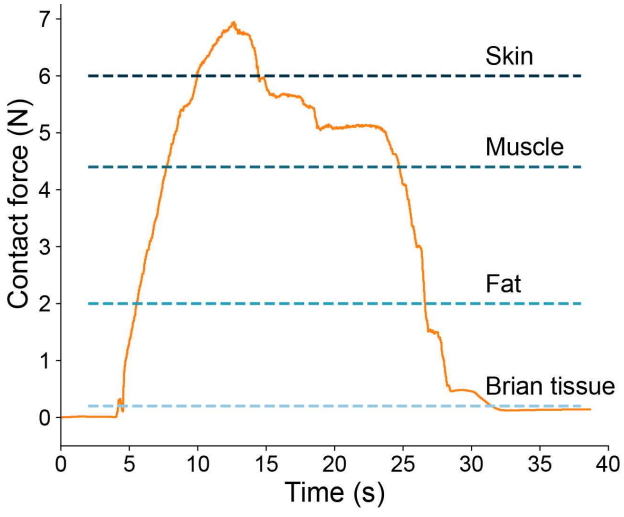

Fig. 7. Contact force profile as the needle driver moves 70% of the stroke length and comparisons with the puncture forces of brain tissue, fat, muscle, and skin.

V. OCT Microneedle Imaging

To validate the accuracy and stability of our robotic system during deep-brain neuroimaging, an OCT imaging microneedle was incorporated into the system and an animal imaging test was performed on a rat brain model. The protocol of OCT imaging in the rat brain was approved by the Laboratory Animal Services Centre at The Chinese University of Hong Kong. A homemade 800-nm spectral-domain OCT (SD-OCT) system was constructed. The configurations and distal imaging optics of the probe are similar to those reported previously [26], [32], [33]. The rigid enclosure was glued to a flexible 500-mm-long torque coil, which was utilized to transfer the rotational torque. A plastic sheath was employed to protect the torque coil, and a glass tube was used to protect the distal optics from the tissues during imaging. The resultant OCT microneedle affords an excellent imaging resolution (2.4 μm×4.5 μm in axial and transverse directions). Furthermore, its ultra-small form size (0.6 mm in outer diameter) minimizes the invasiveness, and thus enhances patient safety by reducing the risk of hemorrhage.

Fig. 8(a) and (b) show the overall robotic and OCT system. The robotic system, containing the needle positioner, needle driver, actuation components, and magnetic tracking system, is shown in Fig. 8(a). The positioner is actuated by cable transmission, which is a part of the double long-distance transmission system for positioning and insertion. The homemade OCT system is shown in Fig. 8(b). The OCT microneedle is connected to a rotary joint which is mounted on a translational stage, making a three-dimensional imaging unit (left of Fig. 8(b)). The imaging unit is connected to the OCT engine for generating the OCT interferometric signal (right of Fig. 8(b)). Fig. 8(c) depicts that the needle driver was attached to the needle positioner, as explained in section II. The OCT imaging micro-needle is incorporated into the robotic system by fitting the rigid part of the microneedle into the needle driver of the robotic platform. The locker on the platform holds the microneedle and makes it move with the needle driver. An oblique view of the OCT micro-needle and a photograph of the microneedle tip under a microscope are showcased in Fig. 8(d).

Before the imaging test, a burr hole was drilled on the skull to allow microneedle deployment. To prevent potential damage to major blood vessels, the point for the burr hole was carefully chosen. The positioner was supported by a universal holder for demonstration. The needle driver was then installed on the platform. After that, the OCT microneedle was fitted into the needle driver. The needle locker was pushed down on the needle holder to tighten the needle holder and the microneedle. The overall installation time of the robot and the microneedle took less than 2 minutes. Once the microneedle was entirely in place, it became stable and less prone to damage due to the protection of the needle guide. The burr hole was first randomly placed in the workspace of the robotic system, and then the positioning and orientation of the microneedle could be readily adjusted towards the burr hole under the guidance of the Electromagnetic (EM)

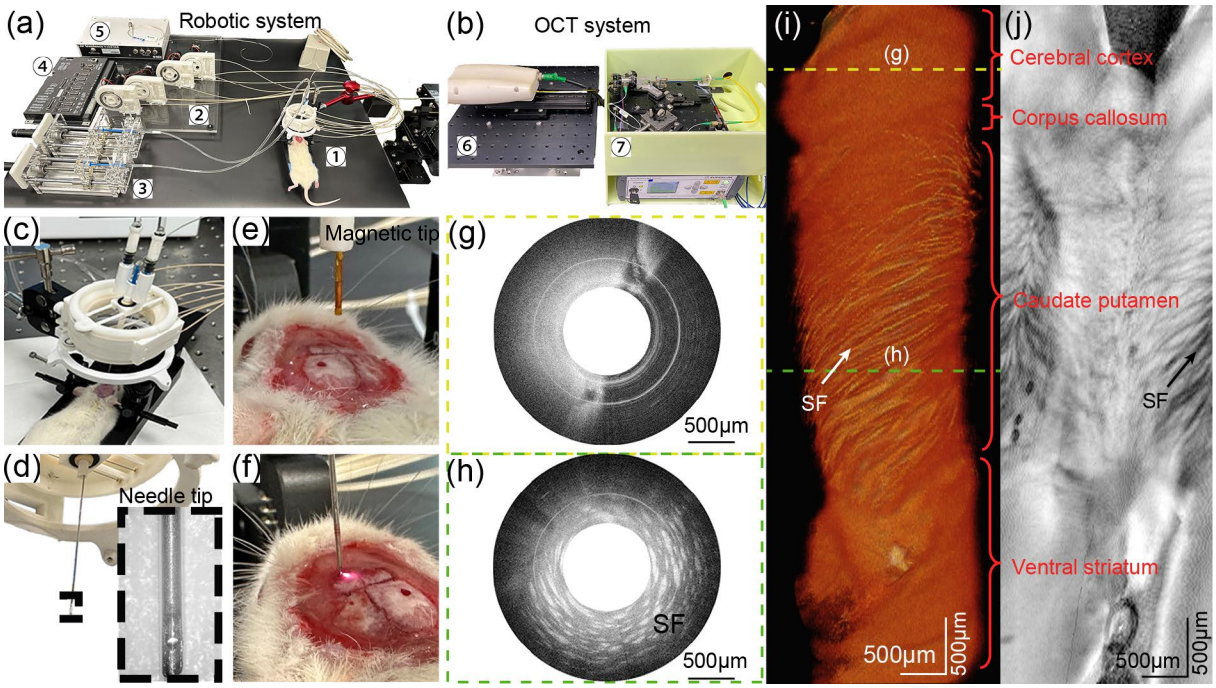

Fig. 8. Head-mounted robotic needle intervention for in vivo OCT neuroimaging in a normal rat brain. (a) The robotic system. ① The needle intervention robot comprises of the needle driver and the positioner. ② Actuation of the positioner. ③ Actuation of the needle driver. ④ Motion controller. ⑤ EM Tracker system. (b) The OCT imaging system. ⑥ OCT imaging micro-motion stage. ⑦ OCT engine. (c) The needle intervention robot was placed over the rat brain. (d) The OCT microneedle with a close-up view. (e) The EM tracker tip moved towards the burr hole. (f) The OCT microneedle end pointed towards the burr hole before insertion. (g) A typical cross-sectional OCT image before the deployment of microneedle into rat brain. (h) A typical cross-sectional OCT image of a rat brain. The white-dotted structures show the characteristic microstructures of striatopallidal fibers (SF). (i) The reconstructed volumetric OCT image of rat brain. The horizontal green dashed lines correspond to the cross-sectional images. Four representative areas are identified. CeCo:Cerebral cortex, CoCa:Corpus callosum, CP:Caudate putamen, VS:Ventral striatum. (j) The en face projection view of the unwrapped brain image. All the scale bars in the image are 500 μm.

tracking system (3D Guidance trakSTAR, NDI Measurement Sciences Inc). Once the imaging microneedle was appropriately positioned, the positioning system was locked. Fig. 8(e) and (f) show the moment when the magnetic tip and OCT microneedle tip moved towards the burr hole, respectively. Held by the needle driver, the OCT microneedle could move along the designed trajectory through the burr hole at a steady speed of 0.5 mm/s and successfully deployed in the rat brain at a predetermined depth of 6 mm.

After the OCT microneedle was deployed in the brain, pull-back imaging was performed to obtain the OCT images at 10 frames per second. A total of 500 frames were obtained within 50 s, and the total imaging depth along the designed trajectory was 5 mm. Two representative cross-sectional images are illustrated in Fig. 8(g) and (h), respectively, before and after complete deployment in the brain, which are also labeled in the reconstructed three-dimensional volumetric image (Fig. 8(i)). In Fig. 8(h), The en face projection view of the unwrapped brain image shows the typical subtle microstructures of striatopallidal fibers in the caudate putamen, indicating the ultrahigh-resolution imaging capability of the OCT microneedle. It is noted that these fibers can also be appreciated in the cross-sectional and volumetric images. The overall imaging experiment has demonstrated that our system can perform a complete set of OCT scans.

VI. Conclusion and Future Work

In this study, we developed a new needle driver and integrated it with a needle positioner and OCT microneedle in a compact and lightweight head-mounted robot. The experimental results have demonstrated that hydraulic transmission provides effective force transmission and high insertion accuracy, matching that of existing MRI-compatible robot [34]. The function of minimally invasive robotic needle intervention has been demonstrated using an OCT microneedle to acquire high-quality cross-sectional and 3D volumetric images of a rat brain.

Building upon our current work, our future research will concentrate on developing a neurosurgical robotic system that leverages OCT scanning and diverse surgical imaging data to enhance minimally invasive procedures in the deep brain. We will further optimize the needle driver and develop an autonomous neuronavigation framework to achieve an automated neurosurgical robot of improved robustness and safety. One motor design will be investigated for more synchronized actuation. Integrating high-resolution OCT neuroimaging information into robot servo control and navigation framework will also help enhance the robots' capabilities in complex deep brain scenarios. Following the current MRI-compatible design, we plan to explore a generic multimodal surgical image-guided-navigation framework to handle different surgical needs.

REFERENCES

[1] M. C. Dewan, A. Rattani, G. Fieggen, M. A. Arraez, F. Servadei, F. A. Boop, W. D. Johnson, B. C. Warf, and K. B. Park, "Global neurosurgery: The current capacity and deficit in the provision of essential neurosurgical care. executive summary of the global neurosurgery initiative at the program in global surgery and social change," *Journal of Neurosurgery*, vol. 130, Apr. 2018.

[2] O. Khanna, R. Beasley, D. Franco, and S. DiMaio, "The path to surgical robotics in neurosurgery," *Operative Neurosurgery*, vol. 20, June 2021.

[3] Y. Xian, X. Zhang, X. Luo, J. Li, L. Zou, K. Xie, J. Li, Y. Li, Y. Huang, D. T. M. Chan, D. Y. C. Chan, and Z. Li, "A semi-autonomous stereotactic brain biopsy robotic system with enhanced surgical safety and surgeon-robot collaboration," *IEEE Transactions on Biomedical Engineering*, 2023.

[4] R. Elsabeh, S. Singh, J. Shasho, Y. Saltzman, and J. M. Abrahams, "Cranial neurosurgical robotics," *British Journal of Neurosurgery*, vol. 35, Sept. 2021.

[5] B. Yang, S. Roys, U.-X. Tan, M. Philip, H. Richard, R. P. Gullapalli, and J. P. Desai, "Design, development, and evaluation of a master–slave surgical system for breast biopsy under continuous MRI," *The International Journal of Robotics Research*, vol. 33, Apr. 2014.

[6] N. A. Patel, G. Li, W. Shang, M. Wartenberg, T. Heffter, E. C. Burdette, I. Iordachita, J. Tokuda, N. Hata, C. M. Tempany, *et al.*, "System integration and preliminary clinical evaluation of a robotic system for MRI-guided transperineal prostate biopsy," *Journal of Medical Robotics Research*, vol. 4, no. 02, p. 1950001, 2019.

[7] M. Friebe, J. Sanchez, S. Balakrishnan, A. Illanes, Y. Nagaraj, R. Odenbach, M. Matooq, G. Krombach, M. Vogele, and A. Boese, "In-room ultrasound fusion combined with fully compatible 3d-printed holding arm–rethinking interventional MRI," *Medical Devices: Evidence and Research*, pp. 77–85, 2018.

[8] G. Li, N. A. Patel, A. Melzer, K. Sharma, I. Iordachita, and K. Cleary, "MRI-guided lumbar spinal injections with body-mounted robotic system: cadaver studies," *Minimally Invasive Therapy & Allied Technologies*, vol. 31, no. 2, pp. 297–305, 2022.

[9] Z. He, Z. Dong, G. Fang, J. D.-L. Ho, C.-L. Cheung, H.-C. Chang, C. C.-N. Chong, J. Y.-K. Chan, D. T. M. Chan, and K.-W. Kwok, "Design of a percutaneous MRI-guided needle robot with soft fluid-driven actuator," *IEEE Robotics and Automation Letters*, vol. 5, no. 2, pp. 2100–2107, 2020.

[10] Z. Wang, Y. Dong, Y. Fang, M. Li, T. Xu, and Y. Lei, "A lightweight high-accuracy 4-DoF robot for CT-image guided percutaneous interventions," in *2022 International Symposium on Medical Robotics (ISMR)*, pp. 1–6, IEEE, 2022.

[11] D. Navarro-Alarcon, S. Singh, T. Zhang, H. L. Chung, K. W. Ng, M. K. Chow, and Y. Liu, "Developing a compact robotic needle driver for MRI-guided breast biopsy in tight environments," *IEEE Robotics and Automation Letters*, vol. 2, no. 3.

[12] X. Xiao, H. Gao, C. Li, L. Qiu, K. S. Kumar, C. J. Cai, B. S. Bhola, N. K. K. King, and H. Ren, "Portable body-attached positioning mechanism toward robotic needle intervention," *IEEE/ASME Transactions on Mechatronics*, vol. 25, Apr. 2020.

[13] H. Gao, X. Xiao, L. Qiu, M. Q.-H. Meng, N. K. K. King, and H. Ren, "Remote-center-of-motion recommendation toward brain needle intervention using deep reinforcement learning," in *2021 IEEE International Conference on Robotics and Automation (ICRA)*, May 2021.

[14] B. Su, S. Yu, H. Yan, Y. D. Hu, I. Buzurovic, D. Liu, L. Liu, Y. Teng, J. Tang, J. Wang, *et al.*, "Biopsy needle system with a steerable concentric tube and online monitoring of electrical resistivity and insertion forces," *IEEE Transactions on Biomedical Engineering*, vol. 68, no. 5, pp. 1702–1713, 2021.

[15] K.-H. Lee, K. C. D. Fu, Z. Guo, Z. Dong, M. C. W. Leong, C.-L. Cheung, A. P.-W. Lee, W. Luk, and K.-W. Kwok, "MR safe robotic manipulator for MRI-guided intracardiac catheterization," *IEEE/ASME Transactions on Mechatronics*, vol. 23, Apr. 2018.

[16] C. C. Nguyen, T. Teh, M. T. Thai, P. T. Phan, T. T. Hoang, J. Davies, H.-P. Phan, C. H. Wang, N. H. Lovell, and T. N. Do, "A handheld hydraulic soft robotic device with bidirectional bending end-effector for minimally invasive surgery," *IEEE Transactions on Medical Robotics and Bionics*, 2023.

[17] S. Frishman, A. Kight, I. Pirozzi, M. C. Coffey, B. L. Daniel, and M. R. Cutkosky, "Enabling in-bore MRI-guided biopsies with force feedback," *IEEE transactions on haptics*, vol. 13, no. 1, pp. 159–166, 2020.

[18] R. Kokes, K. Lister, R. Gullapalli, B. Zhang, A. MacMillan, H. Richard, and J. P. Desai, "Towards a teleoperated needle driver robot with haptic feedback for RFA of breast tumors under continuous MRI," *Medical Image Analysis*, vol. 13, June 2009.

[19] S. Dehghani, M. Sommersperger, P. Zhang, A. Martin-Gomez, B. Busam, P. Gehlbach, N. Navab, M. A. Nasseri, and I. Iordachita, "Robotic navigation autonomy for subretinal injection via intelligent real-time virtual iOCT volume slicing," in *2023 IEEE International Conference on Robotics and Automation (ICRA)*, May 2023.

[20] G. D. Giudice, A. L. Orekhov, J.-H. Shen, K. M. Joos, and N. Simaan, "Investigation of micromotion kinematics of continuum robots for volumetric OCT and OCT-guided visual servoing," *IEEE/ASME Transactions on Mechatronics*, vol. 26, Oct. 2021.

[21] M. Draelos, G. Tang, B. Keller, A. Kuo, K. Hauser, and J. A. Izatt, "Optical coherence tomography guided robotic needle insertion for deep anterior lamellar keratoplasty," *IEEE Transactions on Biomedical Engineering*, vol. 67, July 2020.

[22] J. Wang, C. Xu, S. Zhu, D. Chen, H. Qiu, A. K. N. Lam, C. K. S. Leung, and W. Yuan, "A generic and effective system dispersion compensation method: Development and validation in visible-light OCT," *Photonics*, vol. 10, no. 8, 2023.

[23] W. Yuan, J. Thiboutot, H. C. Park, A. Li, J. Loube, W. Mitzner, L. Yarmus, R. H. Brown, and X. Li, "Direct visualization and quantitative imaging of small airway anatomy in vivo using deep learning assisted diffractive OCT," *IEEE Transactions on Biomedical Engineering*, vol. PP, pp. 1–9, 2022.

[24] J. Thiboutot, W. Yuan, H.-c. Park, D. Li, J. Loube, W. Mitzner, L. Yarmus, X. Li, and R. H. Brown, "Visualization and validation of the microstructures in the airway wall in vivo using diffractive optical coherence tomography," *Academic radiology*, vol. 29, no. 11, pp. 1623–1630, 2022.

[25] W. Yuan, Y. Feng, D. Chen, P. Gharibani, J. D. Chen, H. Yu, and X. Li, "In vivo assessment of inflammatory bowel disease in rats with ultrahigh-resolution colonoscopic oct," *Biomedical optics express*, vol. 13, no. 4, pp. 2091–2102, 2022.

[26] W. Yuan, D. Chen, R. Sarabia-Estrada, H. Guerrero-Cázares, D. Li, A. Quiñones-Hinojosa, and X. Li, "Theranostic OCT microneedle for fast ultrahigh-resolution deep-brain imaging and efficient laser ablation in vivo," *Science Advances*, vol. 6, Apr. 2020.

[27] K. Liu, C. Zhang, and Z. Sun, "Independent pressure and flow rate control enabled by hydraulic free piston engine," *IEEE/ASME Transactions on Mechatronics*, vol. 24, no. 3, pp. 1282–1293, 2019.

[28] H. Gao, R. Hao, X. Yang, C. Li, Z. Zhang, X. Zuo, Y. Li, and H. Ren, "Modeling and compensation of stiffness-dependent hysteresis for stiffness-tunable tendon-sheath mechanism in flexible endoscopic robots," *IEEE Transactions on Industrial Electronics*, Sept. 2023.

[29] M. Lu, Y. Zhang, C. M. Lim, and H. Ren, "Flexible needle steering with tethered and untethered actuation: Current states, targeting errors, challenges and opportunities," *Ann Biomed Eng*, vol. 51, May 2023.

[30] D. J. van Gerwen, J. Dankelman, and J. J. van den Dobbelsteen, "Needle–tissue interaction forces – A survey of experimental data," *Medical Engineering & Physics*, vol. 34, July 2012.

[31] L. S. Gan, K. Zareinia, S. Lama, Y. Maddahi, F. W. Yang, and G. R. Sutherland, "Quantification of forces during a neurosurgical procedure: A pilot study," *World neurosurgery*, vol. 84, no. 2, pp. 537–548, 2015.

[32] W. Yuan, J. Mavadia-Shukla, J. Xi, W. Liang, X. Yu, S. Yu, and X. Li, "Optimal operational conditions for supercontinuum-based ultrahigh-resolution endoscopic OCT imaging," *Optics Letters*, vol. 41, pp. 250–3, Jan. 2016.

[33] W. Yuan, R. Brown, W. Mitzner, L. Yarmus, and X. Li, "Super-achromatic monolithic microprobe for ultrahigh-resolution endoscopic optical coherence tomography at 800 nm," *Nature Communications*, vol. 8, p. 1531, Nov. 2017.

[34] S. Huang, C. Lou, Y. Zhou, Z. He, X. Jin, Y. Feng, A. Gao, and G.-Z. Yang, "MRI-guided robot intervention—current state-of-the-art and new challenges," *Med-X*, vol. 1, no. 1.